Journal of Biomedical Optics

SPIEDigitalLibrary.org/jbo

In vivo preclinical photoacoustic imaging of tumor vasculature development and therapy

Jan Laufer
Peter Johnson
Edward Zhang
Bradley Treeby
Ben Cox
Barbara Pedley
Paul Beard

In vivo preclinical photoacoustic imaging of tumor vasculature development and therapy

Jan Laufer,[a,b] Peter Johnson,[b,c] Edward Zhang,[a] Bradley Treeby,[a*] Ben Cox,[a] Barbara Pedley,[b,c] and Paul Beard[a,b]
[a]University College London, Department of Medical Physics and Bioengineering, Gower Street, London WC1E 6BT, United Kingdom
[b]University College London, Centre for Advanced Biomedical Imaging, Department of Medicine and Institute of Child Health, Paul O'Gorman Building, 72 Huntley Street, London WC1E 6BT, United Kingdom
[c]University College London, The UCL Cancer Institute, Paul O'Gorman Building, 72 Huntley Street, London WC1E 6DD, United Kingdom

Abstract. The use of a novel all-optical photoacoustic scanner for imaging the development of tumor vasculature and its response to a therapeutic vascular disrupting agent is described. The scanner employs a Fabry-Perot polymer film ultrasound sensor for mapping the photoacoustic waves and an image reconstruction algorithm based upon attenuation-compensated acoustic time reversal. The system was used to noninvasively image human colorectal tumor xenografts implanted subcutaneously in mice. Label-free three-dimensional *in vivo* images of whole tumors to depths of almost 10 mm with sub-100-micron spatial resolution were acquired in a longitudinal manner. This enabled the development of tumor-related vascular features, such as vessel tortuosity, feeding vessel recruitment, and necrosis to be visualized over time. The system was also used to study the temporal evolution of the response of the tumor vasculature following the administration of a therapeutic vascular disrupting agent (OXi4503). This revealed the well-known destruction and recovery phases associated with this agent. These studies illustrate the broader potential of this technology as an imaging tool for the preclinical and clinical study of tumors and other pathologies characterized by changes in the vasculature.
[DOI: 10.1117/1.JBO.17.5.056016]

Keywords: interferometry; photoacoustic; preclinical; tumor.

Paper 11656 received Nov. 23, 2011; revised manuscript received Feb. 28, 2012; accepted for publication Mar. 2, 2012; published online May 21, 2012.

1 Introduction

The blood vessel network of a tumor not only regulates the supply of nutrients and oxygen to the cancer cells, which affects their survival and growth, but also influences the response of the tumor to therapy.[1] *In vivo* preclinical studies of the tumor vasculature are therefore of vital importance in fundamental cancer research and the development of new drugs and other therapies. Imaging modalities such as magnetic resonance imaging and x-ray computed tomography (CT) can provide images of high spatial resolution but typically require contrast agents to visualize the vasculature.[2,3] CT also uses ionizing radiation, which can cause detrimental side effects. Pulse-echo ultrasound[4] and speckle variance tracking[5] have also been used to visualize tumor blood vessels. However, the former requires the use of microbubbles as a contrast agent and the latter relies upon the detection of blood flow and therefore provides limited sensitivity to the slow and often chaotic flow in tumors. Optical methods that rely on ballistic photons, such as transillumination and multiphoton microscopy, and optical coherence tomography, can provide compelling *in vivo* images of tumor vasculature development and therapeutic response.[6–9] However, due to the overwhelming optical scattering exhibited by most soft tissues, their imaging depth is restricted to less than 1 mm. More important, achieving even this limited penetration depth requires the use of a skin flap window chamber, which is invasive and restricts tumor growth to shallow depths (<500 μm). In addition, it provides a microenvironment, particularly in the region adjacent to the imaging window, that is very different to that of subcutaneous or orthotopic tumors and may be less representative of normal tumor development.[10] A further limitation of some optical imaging modalities, such as multiphoton microscopy, is that they require contrast agents in order to visualize the vasculature.

Photoacoustic imaging[11] is an emerging noninvasive technique that offers the prospect of overcoming the limitations of the above modalities. It relies upon the generation of ultrasound through the absorption of low-energy nanosecond laser pulses by tissue chromophores, such as hemoglobin. Thermalization of the optical energy causes rapid heating followed by the emission of broadband acoustic waves, which are detected on the tissue surface using ultrasound receivers. From the detected acoustic signals, images of the absorbed optical energy density, which depend upon the tissue optical properties (principally absorption), can then be reconstructed. The key advantage of photoacoustic imaging is that optical contrast is encoded onto acoustic waves that are scattered much less than photons in tissue. This means that, while retaining the high contrast and spectral specificity associated with optical tissue interactions, it provides much greater penetration depths than purely optical imaging methods that exploit ballistic photons; depths of a few cm with scalable spatial resolution ranging from tens to

*Bradley Treeby is now currently at Australian National University, Research School of Engineering, College of Engineering and Computer Science, Building 115, North Road, Canberra ACT 0200, Australia.

Address all correspondence to: Jan Laufer, Julius Wolff Institut, Charité Universitätsmedizin Berlin, Berlin 13353, Germany. Tel: +4930450539419; Fax: +4930450539918; E-mail: jan.laufer@charite.de.

0091-3286/2012/$25.00 © 2012 SPIE

hundreds of microns (depending on depth) are readily achievable. The absorption-based contrast of photoacoustic imaging makes it particularly well suited to visualizing vascular anatomy without the need for contrast agents due to the strong optical absorption of hemoglobin at visible and near infrared wavelengths. In addition, it can provide functional or physiological information. By acquiring images at multiple wavelengths, quantitative spectroscopic measurements of blood oxygen saturation and hemoglobin concentration[12] can be made, and there is the potential to determine blood flow from photoacoustic Doppler measurements.[13–15]

The ability to noninvasively image deep blood vessel networks suggests photoacoustic imaging has strong potential as a preclinical tool for the *in vivo* characterization of the vasculature of whole subcutaneous tumor xenografts. Preliminary photoacoustic tumor imaging studies have previously been undertaken using scanners based on piezoelectric detectors.[16–20] However, these early studies were limited by modest penetration depth and image quality, the latter making it difficult in some cases to clearly distinguish tumor vascular anatomy from that of normal tissue.

In this study, an all-optical photoacoustic detection technology[21] and a new image reconstruction method[22] employing acoustic time reversal that overcomes these limitations is described. This approach provides high-resolution three-dimensional (3-D) photoacoustic images of the vasculature of entire subcutaneous tumors and is shown to be capable of revealing tumor-specific vascular features. This has been demonstrated by imaging, for the first time using photoacoustic techniques, the temporal evolution of two different human colorectal tumor xenografts and their response to a therapeutic vascular disrupting agent. Section 2 describes the imaging instrumentation, image reconstruction method, and *in vivo* imaging protocol, while Sec. 3 presents the images of tumor vasculature development and response to treatment.

2 Methods

2.1 *Small Animal Photoacoustic Imaging System*

In this study, the tomography rather than microscopy mode of photoacoustic imaging was employed.[11] This approach uses full field illumination to irradiate a relatively large volume of tissue and a reconstruction algorithm to form the image from the detected photoacoustic signals. It is the most general and least restrictive photoacoustic imaging approach; it provides greater penetration depth than optical resolution photoacoustic microscopy,[23] which is limited to a maximum depth of ~1 mm, and, unlike acoustic resolution photoacoustic microscopy,[24] it provides acoustic diffraction limited spatial resolution over the entire 3-D field of view.[11]

A detailed description of the imaging system, a schematic of which is shown in Fig. 1(a), can be found in Refs. 21, 25–27. Briefly, it comprises a pulsed laser system for generating the photoacoustic waves and an all-optical scanner based upon a Fabry-Perot (FP) ultrasound sensor for detecting them. The laser system was a fiber-coupled wavelength-tunable optical parametric oscillator (OPO) laser system (premiScan, GWU and Quanta-Ray PRO-270, Newport Spectra Physics) that provided 7 ns pulses at a repetition frequency of 50 Hz. The divergent beam emerging from the optical fiber is directed onto the FP sensor head, which is acoustically coupled to the skin surface via an aqueous gel. The diameter of the beam incident on the sensor is 2 cm. The FP sensor consists of a wedged polymer substrate onto which two dichroic mirrors separated by a 40-μm-thick Parylene C polymer spacer are deposited,[21] thereby forming a Fabry-Perot interferometer (FPI). The mirrors are designed to be transparent in the wavelength range 590 to 1200 nm, but highly reflective between 1500 and 1600 nm. This allows excitation laser pulses in the former wavelength range to be transmitted through the sensor head into the adjacent

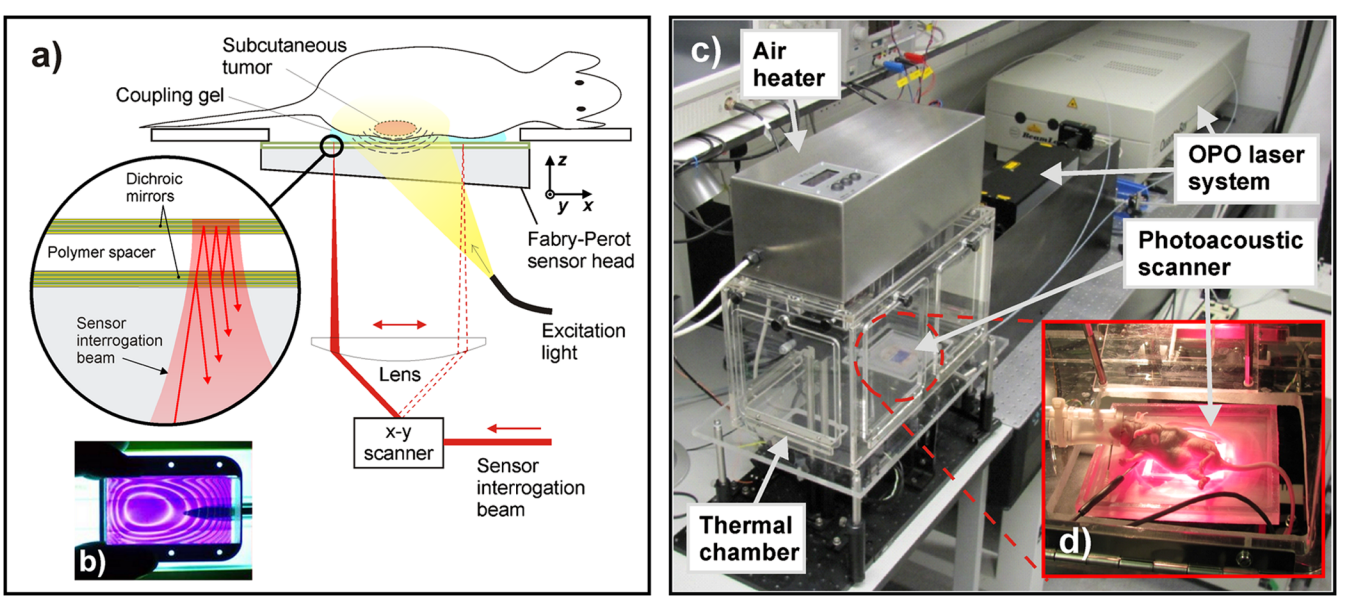

Fig. 1 Small animal photoacoustic imaging system. (a) Schematic illustrating the operation of the system. Photoacoustic waves are generated by the absorption of nanosecond optical pulses provided by a wavelength-tunable OPO laser system and detected by a transparent Fabry-Perot polymer film ultrasound sensor. The waves are mapped in 2-D by raster-scanning a cw focused interrogation laser beam across the sensor and recording the acoustically-induced modulation of the reflectivity of the FPI at each scan point. (b) Photograph of sensor head under narrowband visible illumination illustrating the transparent nature of the sensor. (c) Photograph of the imaging system. (d) The system in operation, showing the anaesthetized animal located on the Fabry-Perot sensor, through which the excitation laser pulses are transmitted.

target tissue. Absorption of the laser energy in the tissue produces photoacoustic pulses that propagate back to the sensor, where they modulate the optical thickness of the FPI and hence its reflectivity. The sensor is read-out by raster scanning a 1550-nm focused interrogation laser beam over its surface using a galvanometer based *x*-*y* optical scanner. To achieve optimum sensitivity, the FPI is optimally biased at each point of the scan by tuning the interrogation laser wavelength to the point of maximum slope on the interferometer transfer function (ITF), the relationship between reflected optical power and phase. Under these conditions, an acoustically induced modulation of the optical thickness of the FPI produces a small phase shift that is linearly converted, via the ITF, to a corresponding reflected optical power modulation. This time-varying power modulation, which represents the photoacoustic waveform, is detected by an InGaS photodiode-transimpedance amplifier unit and recorded using a digital storage oscilloscope (DSO). Once a waveform has been acquired at a particular spatial point for a given excitation laser pulse, it is stored within the onboard memory of the DSO. The interrogation laser beam is then moved to the next scan point, the excitation laser is fired, and the FPI biasing procedure repeated. By mapping the sensor output in this way, the two-dimensional (2-D) distribution of acoustic waves incident on the surface of the sensor can be recorded. As illustrated in Fig. 1(c), the entire system was enclosed within a thermal chamber containing an air heater in order to maintain a body temperature of 37°C in the animals.

The thickness of the FP sensor was 40 μm, which provides a detection bandwidth of 22 MHz (−3 dB point). The line spread function (LSF) represents the instrument limited spatial resolution in the absence of tissue acoustic attenuation. The vertical LSF is limited by the detector bandwidth and is 27 μm. The lateral LSF is determined by several parameters such as the step size, scan area aperture, and bandwidth.[21] In this study, the lateral resolution was defined by the relatively large scan step size (either 70 or 100 μm). The peak noise equivalent pressure of the sensor was 0.21 kPa over a measurement bandwidth of 20 MHz. The diameter of the focused interrogation laser beam was 22 μm, which, to a first approximation, defines the acoustic element size. The maximum scan area was 14×14 mm and a typical scan acquired 20,000 waveforms each of 500 points. The image acquisition time was typically 8 min and limited by the 50 Hz pulse repetition frequency of the excitation laser. All the images in this study were acquired without signal averaging and using an incident fluence below the safe maximum permissible exposure (MPE) for skin.[28]

2.2 *Image Reconstruction Algorithm*

3-D images were reconstructed from the detected time-resolved photoacoustic signals using a time-reversal image reconstruction algorithm that compensates for the frequency dependent acoustic attenuation exhibited by soft tissues.[22] The algorithm uses a pseudospectral (*k*-space) acoustic propagation model to simulate the retransmission of the measured acoustic pressure signals into the domain in time-reversed order, which then refocus to give an image of the initial pressure distribution.[29] Attenuation compensation is included via an acoustic equation of state that accounts for acoustic absorption following a frequency power law, which significantly increases image magnitude and resolution, especially at greater depths.[22] The attenuation parameters were set to those of breast tissue,[30] which has an acoustic absorption coefficient of 0.75 dB $\mathrm{MHz}^{-1.5}\,\mathrm{cm}^{-1}$. The sound speed used in the image reconstruction was determined using an autofocus method.[31] This involved using a fast FFT-based reconstruction algorithm without attenuation compensation to reconstruct a number of images using different sounds speeds.[32] A metric related to image sharpness was calculated for each image, and the sound speed corresponding to its maximum was chosen for the final image reconstruction using the attenuation compensating time reversal algorithm. For the images obtained in this study, the determined sound speed was in the range of 1538 to 1543 $\mathrm{m\,s}^{-1}$.

For display purposes, the reconstructed 3-D images were interpolated onto a four times finer mesh in *x* and *y*. To aid visualization of deeper-lying features, the image intensity was normalized with respect to depth using a one-dimensional exponential function to account for optical attenuation. The maximum intensity projections (MIPs) were displayed using a logarithmic image intensity scale and 3-D rendering was accomplished using 3D-Doctor (Able Software Corp).

2.3 *Tumor Imaging Procedure*

Two *in vivo* imaging studies were undertaken. The first involved imaging two different human colorectal adenocarcinoma xenografts, LS174T and SW1222, at different times in order to study their vascular development. These tumor models were chosen on account of their rapid growth and the distinct differences in their vascular architecture, with the SW1222 tumors exhibiting a more regular blood vessel network compared to the LS174T tumour.[33,34] The xenografts were established in the flank of female nude mice (MF1 nu/nu, $N = 4$ per cell line), six to eight weeks of age, by subcutaneous injection of 5×10^6 cells. The animals were anaesthetized using a mixture of isofluorane and oxygen at a concentration of 4% for induction and 1 to 2% for maintenance and a flow rate of 1 l/min. The tumor xenografts were positioned at the centre of the scan area and aqueous gel was inserted between the skin and the FP sensor head to provide acoustic coupling. Body temperature and respiration rate were monitored and maintained constant throughout the experiments. A typical imaging session was completed within less than 2 h after which the animal was allowed to recover. The tumors were imaged on day 7, 8, and 12 after inoculation. The aim of the second study was to characterize the response of the vasculature to a therapeutic vascular disrupting agent OXi4503 (combretastatin A1 diphosphate). This was assessed by imaging the tumors (SW1222, LS174T, $N = 2$ each) before and after (24, 48 h) administration of 40 mg/kg of the agent via intraperitoneal injection. All experiments were conducted in accordance with the guidelines for the welfare and use of animals in cancer research.[35]

3 Results

Figure 2 shows two examples of tumor images obtained using the system. Figure 2(a) shows a volume-rendered 3-D image (see also Video 1) of a subcutaneous tumor (LS174T) acquired eight days post inoculation. Since this tumor was superficial, a relatively short excitation wavelength of 600 nm was chosen to provide the best compromise between penetration depth and contrast. The central, donut-shaped feature of elevated contrast is the tumor, which is surrounded by the vascular network of the skin. Several artery-vein pairs in the skin can also be seen as indicated by the arrows. Smaller blood vessels, such as superficial arterioles and venules, are also discernable in Fig. 2(b), which shows a MIP of the image shown in Fig. 2(a)—a

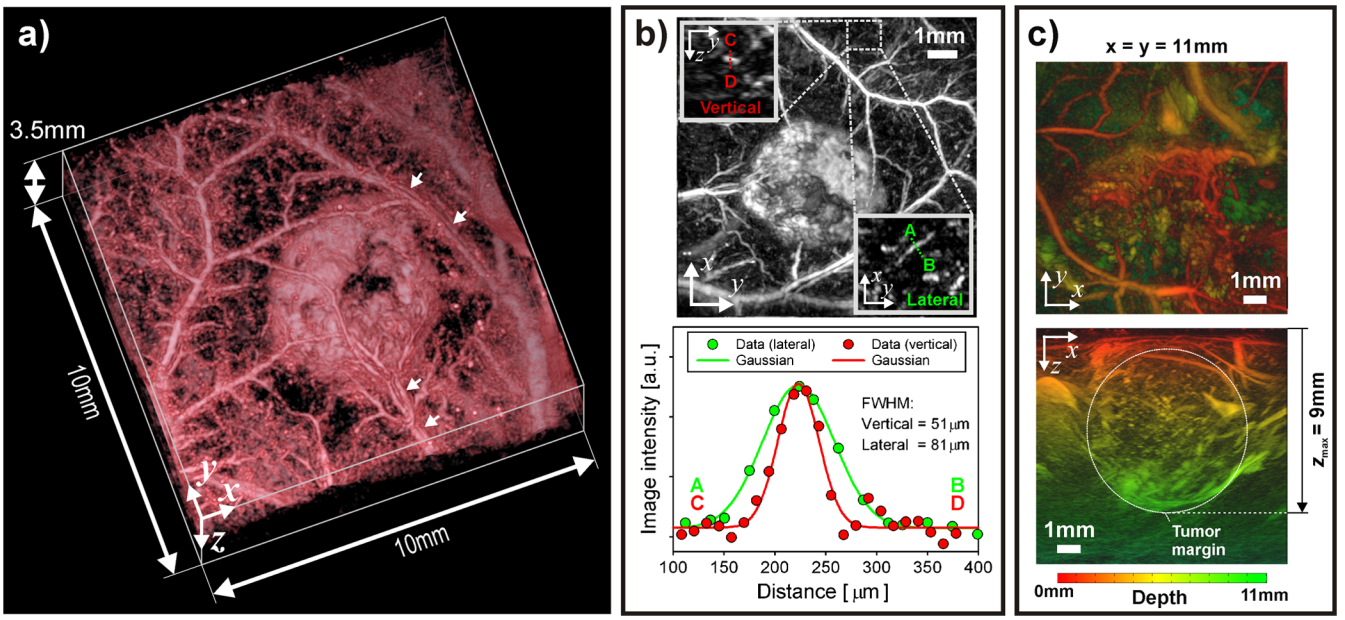

Fig. 2 Photoacoustic images of subcutaneous tumors. (a) Volume-rendered 3-D photoacoustic image of a LS174T tumor (day 8 post inoculation). The image was acquired using an excitation wavelength of 600 nm with a scan step size of 70 μm. The arrows indicate artery-vein pairs. (b) Top: Maximum intensity projection (MIP) of (a). The insets show magnified *y-z* and *x-y* MIPs of a region containing a small blood vessel. To obtain an indication of the spatial resolution, profiles across this vessel between points A-B and C-D were obtained and are plotted in the graph below. The full-width-half-maximum of the profiles was determined from a Gaussian function fitted to the data. (c) *x-y* and *x-z* MIPs of a larger SW1222 tumor (day 12 post-inoculation) illustrating an imaging depth of at least 9 mm. The excitation wavelength was 758 nm. Supplementary information online: volume-rendered 3-D movie of (a), (Video 1, MOV, 4.2 MB). [URL: http://dx.doi.org/10.1117/1.JBO.17.5.056016.1], and a fly-through movie of (b), (Video 2, MOV, 5.6 MB). [URL: http://dx.doi.org/10.1117/1.JBO.17.5.056016.2].

fly-through movie showing successive individual *x-y* slices through the entire data set can also be viewed online (Video 2). The insets in Fig. 2(b) are magnified *x-y* and *y-z* MIPs of a section of the 3-D image containing a small blood vessel at a depth of about 500 μm. To obtain an approximate indication of the spatial resolution, horizontal and vertical profiles through this vessel were obtained and found to be 81 and 51 μm respectively. Figure 2(c) shows *x-y* and *x-z* MIPs of the vasculature of a different tumor (SW1222). This tumor was imaged 12 days after inoculation and had therefore grown to a larger size and extended to a greater depth than the LS174T tumor. For this reason an excitation wavelength of 758 nm, which penetrates more deeply than 600 nm, was used. The *x-z* MIP in Fig. 2(c) shows that the vasculature of this tumor can be visualized to a depth of at least 9 mm. An additional example of a deep-seated tumor (SW1222) is shown in Fig. 3. This shows a well-defined tumor, most evidently in Fig. 3(c), in which the internal tumor vasculature, the subcutaneous tissue surrounding the top surface of the tumor, and the contour of the skin surface can all be visualized.

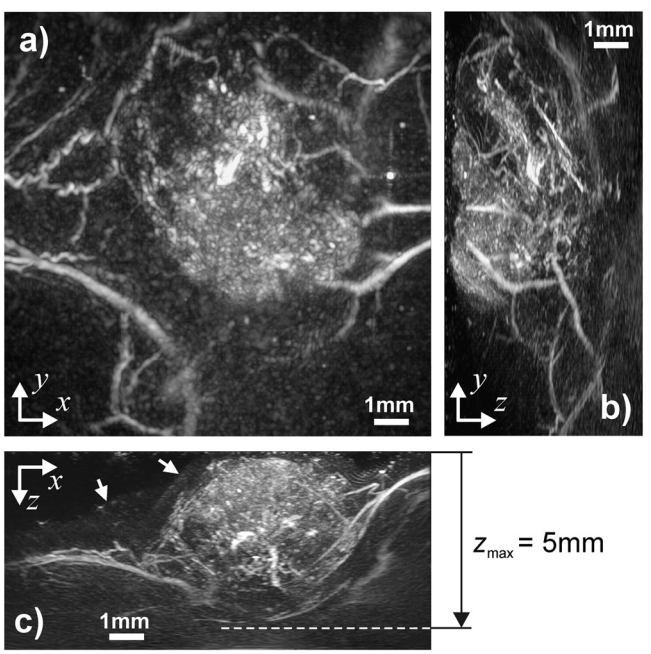

Fig. 3 Photoacoustic image of a subcutaneous SW1222 tumor (day 12 post-inoculation) acquired at a wavelength of 640 nm. (a) *x-y*, (b) *y-z*, and (c) *x-z* maximum intensity projections. The *x-z* and *y-z* MIPs clearly visualize the depth of the tumor. The arrows in (c) indicate the contour of the skin surface.

3.1 *Longitudinal Imaging of Tumor Vascular Development*

Figure 4 shows MIPs of the two human colorectal tumor variants (LS174T, SW1222) acquired at different times between day 7 and day 12 post-inoculation at excitation wavelengths ranging from 600 to 640 nm. The top row of Fig. 4 shows the development of the vasculature within the LS174T tumor and the surrounding tissue. The tumor shows regions of strongly varying contrast, especially towards the tumor centre (days 7 and 8). Since photoacoustic image contrast is mainly due to blood, this is indicative of significant variations in tumor vascularization. The LS174T tumor also produced a noticeable decrease in absorption from day 8 to day 12, which suggests a reduced blood content or possibly tumor necrosis. These findings are

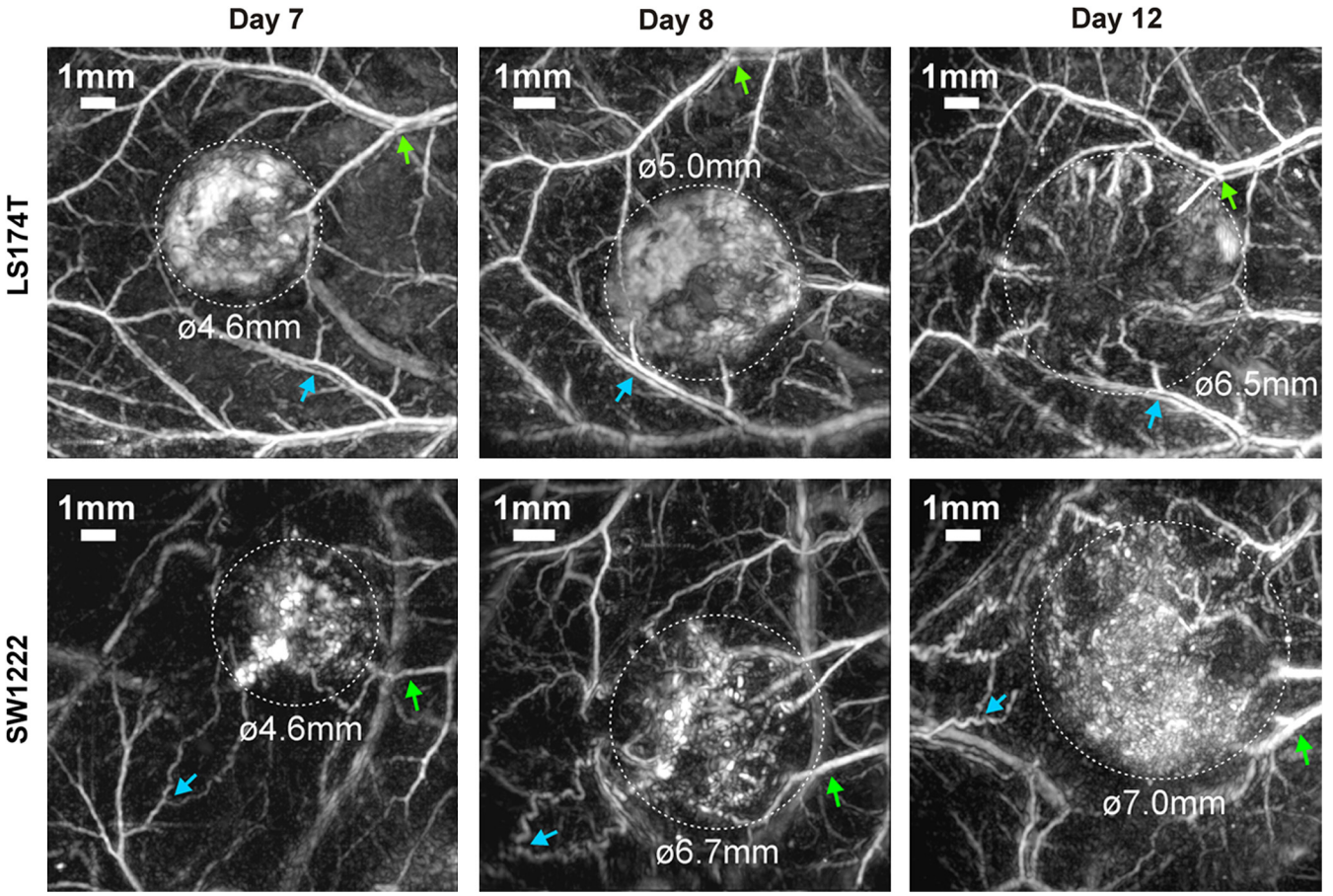

Fig. 4 Photoacoustic images (*x-y* MIPs) showing the development of two types of human colorectal tumor (LS174T, SW1222) and the surrounding vasculature between day 7 and day 12 post-inoculation. The dashed lines indicate the tumor margins. The arrows show common vascular features in the images. The images of the SW1222 tumor (bottom row) also show an increasing tortuosity of previously normal blood vessels (blue arrows). Supplementary information online: 1. Volume-rendered 3-D movie of LS174T, day 7 (Video 3, MOV, 1.7 MB). [URL: http://dx.doi.org/10.1117/1.JBO.17.5.056016.3], 2. Fly-through movie of LS174T, day 8 (Video 2, MOV, 5.6 MB). [URL: http://dx.doi.org/10.1117/1.JBO.17.5.056016.2].

broadly consistent with those of previous stereoimaging and microcomputed tomography studies[33] of vascular corrosion casts, which have shown that LS174T tumors are associated with a heterogeneous vascular distribution, that can also include avascular regions. By contrast, the photoacoustic images of the SW1222 tumor (bottom row) suggest the development of a more homogeneous vasculature. This is also in accordance with previous corrosion cast imaging studies[33] of this type of tumor, which show a more densely packed blood vessel network and a more homogeneous vessel diameter distribution than the LS174T tumor. These studies also reported an increase in the tortuosity of the normal vasculature surrounding the tumor, which has been linked to the emission of tumor growth factors.[33] This feature can be observed in some of the vessels in the photoacoustic images of the SW1222 tumor shown in Fig. 4. For example, the blue arrows in the lower row of Fig. 4 identify a pair of blood vessels that exhibit an increase in tortuosity between day 7 and day 8. The volumes of both tumors, which were estimated from measurements of the tumor length, width, and height,[36] were found to increase by approximately 50% per day over the study duration.

Tumor growth is associated with the recruitment of feeding vessels from the surrounding healthy tissue. This process, which is caused by the emission of growth factors by the tumor cells,[37] can be observed in the photoacoustic images. Figure 5 shows closeups of two MIPs from Fig. 4 (LS174T, days 7 and 12). Over a period of five days, the margin of the tumor (indicated by a dashed line) has not only grown closer to blood vessels in the skin, but the tumor also appears to have integrated some of them as feeding vessels (red arrows, day 12).

3.2 *Photoacoustic Imaging of the Effects of a Vascular Disrupting Agent on the Tumor Vasculature*

To illustrate the potential of photoacoustic imaging for evaluating vascular targeting therapies, images of the vasculature of an LS174T tumor were obtained before and 24 and 48 h after the administration of a vascular disrupting agent.[9,38,39] The vascular disrupting agent used was OXi4503 (combretastatin A1 diphosphate). This selectively blocks and destroys tumor vasculature, resulting in extensive central necrosis. The time course of effects of the combretastatins on tumor vasculature has been documented in studies using microvascular resin casting and histology,[38,40,41] MRI,[42] and *in vivo* confocal microscopy in skin flap window chamber models.[9,40] These studies indicate that post-treatment changes within the tumor can be divided into two phases: a destruction phase within the first 6 to 8 h followed by a recovery phase.[9] The destruction phase is characterized by rapid vascular shutdown and extensive vessel

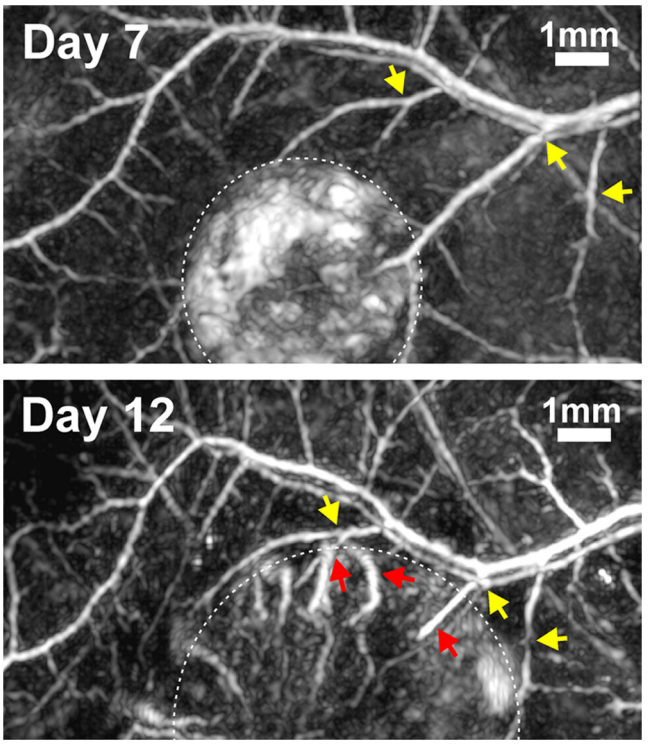

Fig. 5 Photoacoustic images (*x-y* MIPs) of an LS174T tumor showing the development of the tumor vasculature and the recruitment of feeding vessels from the surrounding normal tissue over a period of five days. The dashed line indicates the margin of the tumor within which the development of the tumor blood vessel network can be observed. The yellow arrows indicate common features in the normal blood vessel network. Some of the vessels in this network (indicated by the red arrows) appear to have been recruited by the tumor as feeding vessels by day 12.

disintegration. This results in strongly decreased perfusion particularly at the tumor core[38,42] and an increase in hypoxia[38] and cell death. However, the cells and vessels in the rim of the tumor (the thickness of the rim is approximately 250 to 500 μm) remain intact and functional.[9,38] This allows the recovery phase to commence (>6 to 8 h post-treatment) in the rim and typically results in a gradual increase in its vascular perfusion and a subsequent reduction in hypoxia. At 24 h post-treatment, the tumor core has nevertheless become necrotic[40] due to the lack of nutrients and oxygen. By contrast, the pathophysiological conditions in the tumor rim have not only returned to normal but rapid neovascularization and vascular remodeling is in progress.[9]

The photoacoustic images are broadly consistent with these findings. Figure 6 shows images of an LS174T tumor acquired before and after the administration of OXi4503. Figure 6(a) shows a volume-rendered 3-D image of the tumor obtained pre-treatment. Figure 6(b) shows a subset of the same data but represented as an *x-y* MIP over the depth range $z = 0.8$ to 2.0 mm that was selected to coincide with the center of the tumor in the z direction. Figure 6(c) and 6(d) shows *x-y* MIPs over the same depth range obtained 24 h and 48 h post-treatment. As shown in Fig. 6(b), the contrast distribution in the tumor indicates that it possesses an internal vascular structure before the treatment. Figure 6(c) shows the same tumor section 24 h after treatment. The contrast of the tumor core is now much reduced due to the disintegration of the vasculature produced by the OXi4503. The tumor rim, however, exhibits strong image contrast, suggesting an increase in hemoglobin concentration caused by the reperfusion of blood vessels that had become blocked during treatment[9] but had not disintegrated (a process that is more marked in the rim). After 48 h, the tumor core shows a slight, diffusely distributed increase in image intensity [Fig. 6(d)]. This may indicate an accumulation of hemoglobin due to the reperfusion of vessels in the rim that had partially disintegrated during treatment. Leakage from these vessels into the center can lead to the formation of "vascular lakes."[40]

4 Discussion

This study has shown that the combination of an all-optical photoacoustic scanner and a time-reversal image reconstruction method can provide high-fidelity 3-D *in vivo* images of tumor vasculature to depths of almost 10 mm with sub-100 μm spatial resolution. The enhanced image quality achieved in this study

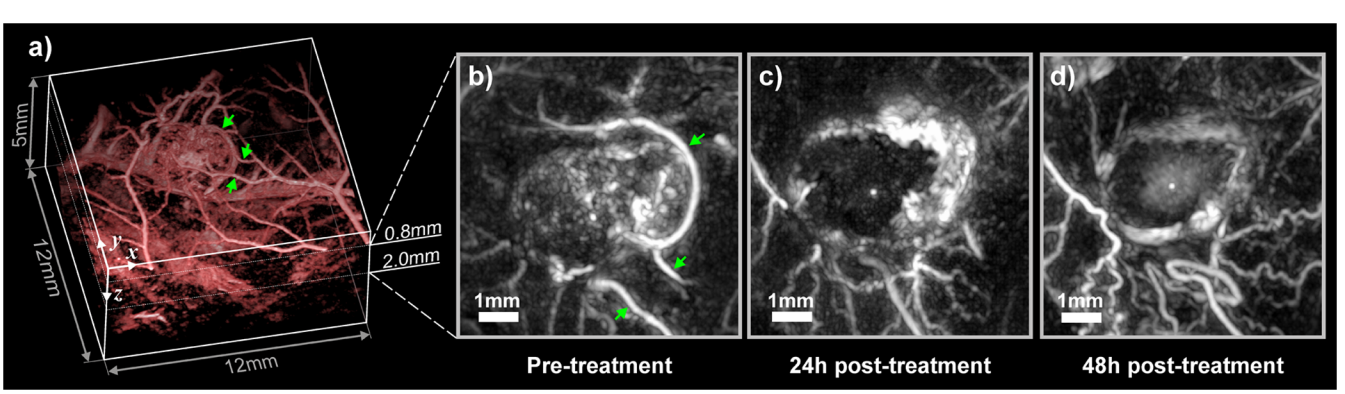

Fig. 6 Photoacoustic images showing the effect of a vascular disrupting agent (OXi4503) on the blood vessel network of a tumor (LS174T). (a) 3-D volume-rendered image of the tumor and the surrounding region prior to the administration of the OXi4503. *x-y* MIPs through the center of the tumor (b) before, (c) 24 h, and (d) 48 h after treatment for $z = 0.8$ to 2.0 mm. The green arrows in (a) and (b) indicate common vascular features in the skin. Some of these blood vessels are not visible in the images obtained 24 h and 48 h post-treatment due to the movement of the skin relative to the tumor. All images were acquired at an excitation wavelength of 640 nm. Supplementary information online: Fly-through movies of LS174T, pre-treatment (Video 4, MOV, 4.1 MB). [URL: http://dx.doi.org/10.1117/1.JBO.17.5.056016.4], 24 h post-treatment (Video 5, MOV, 2.8 MB). [URL: http://dx.doi.org/10.1117/1.JBO.17.5.056016.5], and 48 h post-treatment (Video 6, MOV, 2.0 MB). [URL: http://dx.doi.org/10.1117/1.JBO.17.5.056016.6]).

compared to that provided by previous photoacoustic scanners based on piezoelectric detectors operating in tomography mode is a consequence of several factors. First, the FP sensor provides exceptional broadband acoustic performance. In particular, compared to a similarly broad-banded piezoelectric ultrasound receiver of sub-100-μm element diameter (as required for high resolution imaging to depths of up to ~10 mm in tomography mode), the FP sensor can provide two orders of magnitude higher sensitivity yielding higher image SNR and penetration depth.[21] Second, the compensation for frequency dependent acoustic attenuation that the time-reversal image reconstruction algorithm provides yields higher spatial resolution and contrast than noncompensated methods usually used in photoacoustic imaging. A further advantage, albeit one that relates more to ease of operation than imaging performance, derives from the transparent nature of the sensor head. This provides a true backward mode photoacoustic imaging configuration that allows straightforward delivery of the excitation light and convenient interfacing of the instrument to the animal.

The practical utility of the system as a tool for studying tumor vasculature has been demonstrated by undertaking two specific *in vivo* longitudinal imaging studies. The first involved acquiring 3-D *in vivo* images of two different colorectal tumor xenografts at different time points during their development. This showed that architectural vascular features characteristic of each tumor type could be observed. It also showed that dynamic changes such as variations in tumor vascularization, vessel tortuosity, vessel recruitment, and necrosis that are known to accompany tumor development could be followed over time. In the second study, *in vivo* photoacoustic images of a tumor before and after treatment with a vascular disrupting agent were acquired. These images demonstrated that features characteristic of the well-established destruction and recovery phases associated with this agent could be followed over time. In both studies, the observed changes in vascular morphology, although known from histological studies, have not previously been visualized *in vivo* and wholly noninvasively (i.e., without using a window chamber and/or contrast agents) by any imaging modality to the depths reported in this study. As well as being of interest in their own right, these studies serve also to illustrate the broader potential of the technology for studying angiogenesis and other pathophysiological processes implicated in tumor development, evaluating vascular targeting therapies, and elucidating the role of tumor vasculature as a prognostic biomarker.

In summary, it is considered that this type of photoacoustic imaging instrument may find application as a preclinical tool for studying the pathophysiology of tumors and their response to antivascular treatment. It may also find broader application in preclinical and clinical medicine for studying other pathologies characterized by changes in the structure and function of the vasculature.

Acknowledgments

The authors would like to thank OXiGENE, Inc., for kindly providing the vascular disrupting agent, OXi4503, and Mathew Robson for providing technical help. The authors also wish to acknowledge Mark Lythgoe, Director of the UCL Centre of Advanced Biomedical Imaging, for his help, advice, and providing the infrastructure that allowed this study to be undertaken. This work was supported by King's College London and University College London Comprehensive Cancer Imaging Centre Cancer Research UK & Engineering and Physical Sciences Research Council, in association with the Medical Research Council and Department of Health, UK.

References

1. J. Denekamp, "Inadequate vasculature in solid tumours: consequences for cancer research strategies," *BJR Supplement/BIR* **24**, 111–117 (1992).
2. M.-F. Penet et al., "Molecular and functional MRI of the tumor microenvironment," *J. Nucl. Med.* **49**(5), 687–690 (2008).
3. F. Kiessling et al., "Volumetric computed tomography (VCT): a new technology for noninvasive, high-resolution monitoring of tumor angiogenesis," *Nat. Med.* **10**, 1133–1138 (2004).
4. F. S. Foster, J. Hossack, and S. L. Adamson, "Micro-ultrasound for preclinical imaging," *Interface Focus* **1**(4), 576–601 (2011).
5. Y. Shaked et al., "Therapy-induced acute recruitment of circulating endothelial progenitor cells to tumors," *Science* **313**(5794), 1785–1787 (2006).
6. G. M. Tozer et al., "Intravital imaging of tumour vascular networks using multi-photon fluorescence microscopy," *Adv. Drug Deliv. Rev.* **57**(1), 135–152 (2005).
7. B. J. Vakoc et al., "Three-dimensional microscopy of the tumor microenvironment in vivo using optical frequency domain imaging," *Nat. Med.* **15**, 1219–1223 (2009).
8. G. M. Tozer et al., "Mechanisms associated with tumor vascular shutdown induced by combretastatin A-4 phosphate: intravital microscopy and measurement of vascular permeability," *Cancer Res.* **61**, 6413–6422 (2001).
9. M. Wankhede et al., "In vivo functional differences in microvascular response of 4T1 and Caki-1 tumors after treatment with OXi4503," *Oncol. Rep.* **23**(3), 685 (2010).
10. S. Hak et al., "Intravital microscopy in window chambers: a unique tool to study tumor angiogenesis and delivery of nanoparticles," *Angiogenesis* **13**(2), 113–130 (2010).
11. P. Beard, "Biomedical photoacoustic imaging," *Interface Focus* **1**(4), 602–631 (2011).
12. J. Laufer et al., "Quantitative spatially resolved measurement of tissue chromophore concentrations using photoacoustic spectroscopy: application to the measurement of blood oxygenation and haemoglobin concentration," *Phys. Med. Biol.* **52**(1), 141–168 (2007).
13. J. Yao et al., "In vivo photoacoustic imaging of transverse blood flow by using Doppler broadening of bandwidth," *Opt. Lett.* **35**(9), 1419–1421 (2010).
14. A. Sheinfeld, S. Gilead, and A. Eyal, "Simultaneous spatial and spectral mapping of flow using photoacoustic Doppler measurement," *J. Biomed. Opt.* **15**(6), 066010 (2010).
15. J. Brunker and P. Beard, "Pulsed photoacoustic Doppler flow measurements in blood-mimicking phantoms," *Proc. SPIE* **7899**, 78991K (2011).
16. Y. Lao et al., "Noninvasive photoacoustic imaging of the developing vasculature during early tumor growth," *Phys. Med. Biol.* **53**(15), 4203–4212 (2008).
17. R. I. Siphanto et al., "Serial noninvasive photoacoustic imaging of neovascularization in tumor angiogenesis," *Opt. Express* **13**(1), 89–95 (2005).
18. G. F. Lungu et al., "In vivo imaging and characterization of hypoxia-induced neovascularization and tumor invasion," *Int. J. Oncol.* **30**, 45–54 (2007).
19. G. Ku et al., "Imaging of tumor angiogenesis in rat brains in vivo by photoacoustic tomography," *Appl. Opt.* **44**(5), 770–775 (2005).
20. X. Liang-Zhong et al., "In vivo monitoring of neovascularization in tumour angiogenesis by photoacoustic tomography," *Chin. Phys. Lett.* **24**(3), 751–754 (2007).
21. E. Zhang, J. Laufer, and P. Beard, "Backward-mode multiwavelength photoacoustic scanner using a planar Fabry-Perot polymer film ultrasound sensor for high-resolution three-dimensional imaging of biological tissues," *Appl. Opt.* **47**(4), 561–577 (2008).
22. B. E. Treeby, E. Z. Zhang, and B. T. Cox, "Photoacoustic tomography in absorbing acoustic media using time reversal," *Inverse Probl.* **26**(11), 115003 (2010).

23. K. Maslov et al., "Optical-resolution photoacoustic microscopy for in vivo imaging of single capillaries," *Opt. Lett.* **33**(9), 929–931 (2008).
24. H. F. Zhang et al., "Functional photoacoustic microscopy for high-resolution and noninvasive in vivo imaging," *Nat. Biotechnol.* **24**, 848–851 (2006).
25. J. Laufer et al., "Three-dimensional noninvasive imaging of the vasculature in the mouse brain using a high resolution photoacoustic scanner," *Appl. Opt.* **48**(10), D299–D306 (2009).
26. E. Z. Zhang et al., "Multimodal photoacoustic and optical coherence tomography scanner using an all optical detection scheme for 3D morphological skin imaging," *Biomed. Opt. Express* **2**(8), 2202–2215 (2011).
27. E. Z. Zhang et al., "In vivo high-resolution 3D photoacoustic imaging of superficial vascular anatomy," *Phys. Med. Biol.* **54**(4), 1035–1046 (2009).
28. British standard: safety of laser products BS EN 60825-1 (1994).
29. B. E. Treeby and B. T. Cox, "k-Wave: MATLAB toolbox for the simulation and reconstruction of photoacoustic wave fields," *J. Biomed. Opt.* **15**(2), 021314 (2010).
30. T. L. Szabo, *Diagnostic Ultrasound Imaging*, Elsevier Academic Press, London (2004).
31. B. E. Treeby et al., "Automatic sound speed selection in photoacoustic image reconstruction using an autofocus approach," *J. Biomed. Opt.* **16**(9), 090501 (2011).
32. K. P. Köstli et al., "Temporal backward projection of optoacoustic pressure transients using fourier transform methods," *Phys. Med. Biol.* **46**(7), 1863–1872 (2001).
33. A. A. Folarin et al., "Three-dimensional analysis of tumour vascular corrosion casts using stereoimaging and micro-computed tomography," *Microvasc. Res.* **80**(1), 89–98 (2010).
34. E. El Emir et al., "Predicting response to radioimmunotherapy from the tumor microenvironment of colorectal carcinomas," *Cancer Res.* **67**, 11896–11905 (2007).
35. P. Workman et al., "Guidelines for the welfare and use of animals in cancer research," *Br. J. Cancer* **102**, 1555–1577 (2010).
36. J. P. Feldman et al., "A mathematical model for tumor volume evaluation," *J. Appl. Quant. Methods* **4**(4), 455–462 (2009).
37. N. Ferrara and R. S. Kerbel, "Angiogenesis as a therapeutic target," *Nature* **438**, 967–974 (2005).
38. E. El-Emir et al., "Tumour parameters affected by combretastatin A-4 phosphate therapy in a human colorectal xenograft model in nude mice," *Eur. J. Cancer* **41**(5), 799–806 (2005).
39. R. B. Pedley et al., "Eradication of colorectal xenografts by combined radioimmunotherapy and combretastatin A-4 3–O -phosphate," *Cancer Res.* **61**, 4716–4722 (2001).
40. L. S. Chan et al., "Alterations in vascular architecture and permeability following OXi4503 treatment," *Anti-Cancer Drugs* **19**(1), 17–22 (2008).
41. H. W. Salmon, C. Mladinich, and D. W. Siemann, "Evaluations of vascular disrupting agents CA4P and OXi4503 in renal cell carcinoma (Caki-1) using a silicon based microvascular casting technique," *Eur. J. Cancer* **42**(17), 3073–3078 (2006).
42. H. W. Salmon and D. W. Siemann, "Effect of the second-generation vascular disrupting agent OXi4503 on tumor vascularity," *Clin. Cancer Res.* **12**, 4090–4094 (2006).